Electrochemical hydrogenation of biomass-based furfural in aqueous media by Cu catalyst supported on *N*-doped hierarchically porous carbon

Wanling Xu [a,1], Chunjie Yu [a,b,1], Jinzhu Chen [a,*], Zhiyong Liu [b,*]

[a] *College of Chemistry and Materials Science, Guangdong Provincial Key Laboratory of Functional Supramolecular Coordination Materials and Applications, Jinan University. Guangzhou 511443, China*
[b] *School of Chemistry and Chemical Engineering, Shihezi University/Key Laboratory for Green Processing of Chemical Engineering of Xinjiang Bingtuan/Key Laboratory of Materials-Oriented Chemical Engineering of Xinjiang Uygur Autonomous Region/Engineering Research Center of Materials-Oriented Chemical Engineering of Xinjiang Bingtuan, Shihezi, Xinjiang 832003, China*

A B S T R A C T

Electrochemical hydrogenation (ECH) is a particularly important and environmentally friendly approach to obtain biomass-based fuels and high value-added fine chemicals without using external hydrogen. Herein, we reported a highly efficient and selective ECH of furfural (FF) into furfuryl alcohol (FA) with Cu-based electrocatalyst in aqueous alkaline media. Under the optimal conditions, FA selectivity close to 100% with 99% FF conversion and total Faradaic efficiency above 95% were obtained with the electrocatalyst. Mechanism investigation suggests an ECH mechanism for FA formation, which is highly potential-dependent to FA selectivity, requiring low and well-matched concentrations between active hydrogen (H_{ads}) species and FA radical on the Cu surface. Moreover, the electrocatalyst shows an excellent stability and recyclability during the eight-time consecutive recycling experiments, yielding a total amount of 1011 mg FA. This work thus highlights an important guidance for electrocatalytic upgrading of biomass-based platform molecules in an environmentally friendly way.

1. Introduction

With the increasing environment pollution and energy pinch, the developments in sustainable and renewable energies have attracted great attentions to reduce our dependence on fossil energy [1,2]. In this regard, biomass is currently regarded as carbon-based resource and a renewable energy to replace fossil feedstock for sustainable productions of fuels and chemicals [3,4]. Furfural (FF) is one of the most important biomass-based platform compounds, which is readily obtained by acidolysis of hemicelluloses [5–7]. A variety of high value-added derivatives involving furfuryl alcohol (FA), tetrahydrofurfuryl alcohol, furan, methyl furan, 1,5-pentanediol, furoic acid and furoic ester can be directly obtained from FF *via* hydrogenation, hydrogenolysis, decarbonylation, oxidation, esterification, acidolysis and condensation reactions [8–12]. Among these FF-based derivatives, FA plays a typically important role in the productions of resins, plasticizers, pharmaceutical intermediates, rocket fuel and rubber [13]. Therefore, FF hydrogenation to FA is of great significance in biomass-based transformations.

Currently, FA is industrially obtained from FF with Cu-Cr based catalysts by gas-phase hydrogenation [14]. However, high temperature (above 200 °C) and low selectivity are generally involved in this process [15,16]. Liquid-phase hydrogenation of FF shows an enhanced selectivity, which is also a research hotspot in recent years [17,18]. Various metallic (Cu [19], Ni [20], Pd [21], Ru [22], Pt [23], etc.) and bimetallic catalysts (Cu-Pd [24], Fe-Pd [25], Ni-Al [26], Ni-Mo [27], Pt-Mo [28], etc.) are developed to achieve excellent FA selectivity and FF conversion. While, pressurized hydrogen (2.0–8.0 MPa), moderate reaction temperature (100–200 °C) and the use of volatile organic solvent are generally required for the liquid-phase hydrogenation [29–31]. Therefore, a more sustainable and green way for FF-to-FA upgrading is highly urgent and important [32,33].

Recently, electrochemical hydrogenation (ECH) is developed as an innovative and environmentally friendly method for transformation of biomass-based platform compounds [34–37]. Notably, the ECH process can perform under atmospheric pressure at ambient temperature without using external hydrogen [38–40]. In some cases, water
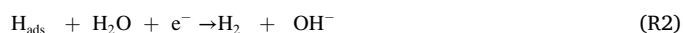
---

* Corresponding authors.
  E-mail addresses: chenjz@jnu.edu.cn (J. Chen), lzyongclin@sina.com (Z. Liu).
[1] These authors contributed equally.

simultaneously functions as both solvent and hydrogen source for the ECH, thus avoiding the use of organic solvent and external/pressurized hydrogen [41–43]. Another advantage of the ECH is that the reaction selectivity can be readily controlled by electrode material (electrocatalyst) electrolysis potential, electrolysis current and electrolyte pH [44,45]. Moreover, ECH shows a great potential for industrial application from the viewpoint of continuous hydrogenation process since the ECH process can run all the time with a continuous transfer of electrons [46,47]. For example, Huber et al. designed a consecutive electrocatalytic membrane reactor for successive production of FA by ECH of FF [48]. Therefore, ECH of FF is a promising and innovative method for FA production from the viewpoint of environment, sustainability and economy.
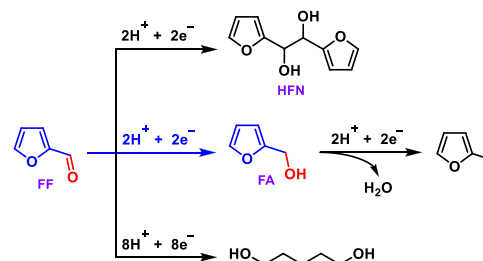
Generally, the research on ECH of FF to FA is still very limited and there are several critical issues involved in the ECH process on the FA selectivity. First, in most cases, the Faradaic efficiency for ECH of FF is low in aqueous media because of the competition reactions between water reduction to H_2 and ECH of FF [49,50]. Therefore, the catalyst with appropriate and moderate electrocatalytic activity is highly desirable to achieve efficient and selective conversion of FF to FA [51]. For example, the electrocatalyst must be able to efficiently catalyze Volmer reaction (reaction R1) to generate adsorbed and active hydrogen (H_{ads}) species in the initial ECH process. However, the subsequent Heyrovsky (reaction R2) or Tafel processes (reaction R3) for H_2 evolution should be significantly suppressed by the electrocatalyst in order to conversely promote the FF reduction [9,52–55].

$$H_2O \ + \ e^- \rightarrow H_{ads} \ + \ OH^- \qquad (R1)$$

$$H_{ads} \ + \ H_2O + e^- \rightarrow H_2 \ + \ OH^- \qquad (R2)$$

$$H_{ads} \ + \ H_{ads} \rightarrow H_2 \qquad (R3)$$

For instance, noble metals, typically Pt, have strong ability for hydrogen evolution reaction (HER) in water splitting, thus leading to a strong competition in the ECH of FF [56]. In contrast, the transition metals with poor catalytic performance in Heyrovsky process are beneficial to the subsequent hydrogenation step [39,57,58]. Among various investigated transition metals, Cu atom has a special outer layer electron arrangement and shows a more suitable redox potential for selective reduction of FF by simultaneously inhibiting the Heyrovsky process [58–61]. For instance, Lin et al. studied the ECH of FF with several transition metals (Cu, Pb, Ni, Fe, Ti, etc) [62]. Among the investigated transition metal electrodes, Cu foil shows the largest positive shift of the onset potential from −1.30 to −1.23 V with significantly increased current density from 0.89 to 3.97 mA cm^{-2} in the presence of 0.1 M FF. Therefore, H_2 formations *via* Heyrovsky or Tafel processes were remarkably suppressed on the surface of Cu electrode, which thus efficiently promotes FF reduction.

Second, plain metal foil electrodes with extremely low surface areas were initially investigated for ECH reaction. The ECH researches on guaiacol, lactic acid and phenol have demonstrated that the cathode with low surface areas generally leads to low conversion level of substrates as well as low selectivity of the desired products due to low reduction rates and mass-transfer limitations. In contrast, Zhang's team recently synthesized a carbon cloth supported Cu$_3$P electrocatalyst with high surface areas as cathode for efficient ECH of FF to FA [63]. The obtained Cu$_3$P with the corresponding Faradaic efficiency up to 95% exhibits higher ECH performance than the reported Cu foil electrode. In addition to its high surface area, it is suggested that heteroatom doping (P, N, O, etc.) can efficiently regulate the electronic structure of the Cu, thus leading to an enhanced ECH activity for FF conversion. Therefore, the development of supported Cu-based electrocatalyst with high surface area can not only significantly reduce the dosage of Cu metal, but also readily regulate its electrocatalytic performance.

Finally, various competing reactions and multiple reaction pathways were observed in the ECH network of FF, which involves the desired

Scheme 1. ECH network of FF.

ECH of FF to FA and undesired reactions such as electrohydrodimerization of FF to hydrofuroin (HFN), electrohydrogenolysis/ring-opening of FF to 1,5-pentanediol, and electrohydrogenolysis of FA to 2-methylfuran (Scheme 1). The HFN comes from electrohydrodimerization of FF, which is generally related to low reduction rate and diffusion rate of FF over the electrode with low surface area. While, the formations of 2-methylfuran and 1,5-pentanediol are usually attributed to electrohydrogenolysis processes in acidic electrolyte. Therefore, it is still a great challenge to achieve high efficiency and selectivity for the desired FA product. Accordingly, rationally designed Cu catalysts with hierarchically porous structure and high surface areas was developed in this research with aqueous alkaline solution as electrolyte for ECH of FF to improve FA selectivity.

Inspired by the above discussion, herein, we reported highly efficient and selective ECH of FF to FA with Cu electrocatalyst (Cu/NC$_{900}$) in aqueous KOH media in an H-type electrolytic reactor at ambient temperature (Fig. 1). The Cu/NC$_{900}$ exhibits highly dispersed Cu species with uniform nanoparticles supported on a three-dimensional (3D) and hierarchically porous carbon framework (NC$_{900}$). The NC$_{900}$ is assembled by highly cross-linked and ultra-thin N-doped carbon nanosheets. Typically, the 15%-Cu/NC$_{900}$ has high surface area of 1641 m^2 g^{-1} showing high electrochemically active surface area (ECSA) of 2261 cm^2 in the ECH of FF. Under the optimal conditions, a FA selectivity close to 100% with Faradaic efficiency above 95% and FF conversion of 99% were obtained with the Cu electrocatalyst. Moreover, the catalyst shows an excellent stability and recyclability during an eight-time consecutive recycling by yielding 1011 mg of FA under the investigated conditions.

2. Experimental section

2.1. Materials

Unless otherwise stated, all chemicals and reagents are directly used as obtained without further purification. 2,4-Dihydroxybenzoic acid, hexamethylenetetramine, ethylenediamine, pluronic P123, melamine, copper nitrate [Cu(NO$_3$)$_2$·3H$_2$O], potassium bicarbonate (KHCO$_3$), potassium hydroxide (KOH), FF and FA were purchased from Aladdin reagent (Shanghai, China). HCl (36–38 wt% aqueous solution) was purchased from Guangzhou KuTai Trading Co., Ltd. Acetone and absolute ethanol were purchased from Guangzhou Chemical Reagent Factory (Guangzhou, China). Nafion solution was purchased from DuPont. All the electrodes were obtained from Shanghai Jingchong Electronic Technology Development Co., Ltd. Deionized water was obtained from Jinan University. High purity gases including H_2/N_2 (V_{H2} 8%), N_2 (99.999%) and liquid nitrogen were purchased from Guangzhou Yinglai Gas Co., Ltd. (Guangzhou, China). NC$_{900}$ was obtained by our previous reported methods [64]. The hydrophilic modification method of carbon cloth and grinding method of glassy carbon electrode will be described in detail below.
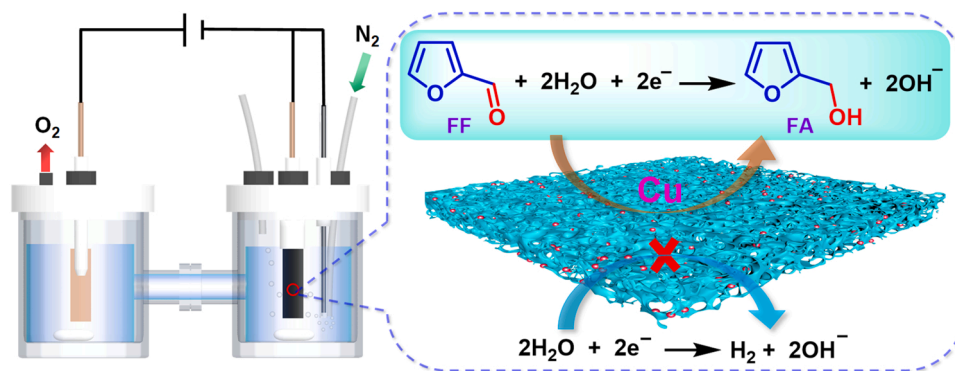
Fig. 1. Cu-catalyzed ECH of FF to FA.

2.2. Preparation of catalyst

2.2.1. Preparation of 15%-Cu/NC$_{900}$

NC$_{900}$ (200 mg), melamine (450 mg), Cu(NO$_3$)$_2$·3H$_2$O (150 mg) and deionized water (80 mL) were well mixed. The resulting mixture was vigorously stirred at ambient temperature for 2 h and at 85 °C for 5 h. The water was then removed from the mixture by a rotary evaporator under reduced pressure. The obtained solid sample was pyrolyzed with the heating rate of 5 °C min^{-1} and then kept at 600 °C for 2 h under an atmospheric H$_2$/N$_2$ (V_{H2} 8%) to give 15%-Cu/NC$_{900}$ (Cu, 15 wt%; about 150 mg).

2.2.2. Preparation of 15%-Cu$^{(II)}$/NC$_{900}$

NC$_{900}$ (200 mg), Cu(acac)$_2$ (62 mg) and methanol (5 mL) were added into a Teflon inner tube in a 25 mL stainless-steel autoclave. Then the sealed autoclave was slowly purged with CO$_2$ for three times, and finally the CO$_2$ was gradually charged into the autoclave. The reaction was performed at 120 °C for 24 h with the pressure of 16 MPa. The autoclave was then slowly cooled down to room temperature after the reaction, 15%-Cu$^{(II)}$/NC$_{900}$ was collected after thoroughly washing with methanol-water and drying under the vacuum (Cu, 15 wt%; about 180 mg).

2.3. Preparation and electrochemical test of electrode

2.3.1. Pretreatment of carbon cloth

Carbon cloth was initially ultrasonicated in a mixture of acetone (20 vol%), ethanol (60 vol%) and water (20 vol%) for 2 h for full cleaning. The obtained carbon cloth was then treated with concentrated nitric acid under reflux conditions for 24 h. Finally, the carbon cloth was cleaned with a mixture-solution of acetone, ethanol and water again, and dried for 12 h under vacuum. The pretreated carbon cloth was then put into anhydrous ethanol for standby.

2.3.2. Pretreatment of glassy carbon electrode

The carbon electrode was grinded step by step with 1.0, 0.3 and 0.05 μm Al$_2$O$_3$ powder.

2.3.3. Preparation of working electrode

The obtained Cu catalyst (5 mg) and Nafion solution (30 μL) were thoroughly dispersed by ultrasonication for half an hour in a mixture of anhydrous ethanol (750 μL) and deionized water (220 μL) to give a uniform catalyst ink. The resulting ink (15 μL) was then slowly dripped onto the surface of glassy carbon electrode (diameter = 3 mm, surface area = 0.07065 cm^2) and dried in air. For electrolytic test, the above catalyst ink (0.6 mL) was uniformly deposited on carbon cloth (1.0 × 1.0 cm) and dried overnight under vacuum at 60 ℃.

2.3.4. Electrochemical test

All electrochemical tests were performed with electrochemical workstation (CHI-760E). An H-type electrolyzer was designed and separated by proton exchange membrane (Fig. 1). The H-type electrolyzer was equipped with an electrolyte of 1.0 M KOH (50 mL) using counter electrode of Pt sheet (1.0 × 1.0 cm) as and reference electrode of Ag/AgCl. The potential obtained from the test was converted into a reversible hydrogen electrode (RHE) by Eq. (1):

$$E(RHE) = E(Ag/AgCl) + 0.059 \times pH + 0.222 \text{ V} \tag{1}$$

The cyclic voltammetry (CV) curves of the non-Faradaic regions were measured by CV, and the electric double layer capacitance (C$_{dl}$) was calculated by Eq. (2):

$$C_{dl} = (j_a\text{-}j_c)/2 \tag{2}$$

where (j_a-j_c) were the differences in current density.

The electrochemically active surface area (ECSA) was obtained by Eq. (3):

$$ECSA = C_{dl}/C_s = C_{dl}/0.04 \tag{3}$$

where C$_s$ was the capacitance measured from ideally smooth, planar surfaces of catalysts, and here we used the typical value of 0.04 mF cm^{-2} for calculation.

2.4. Characterizations

The metal content was analyzed with an Optima 2000 DV inductively coupled plasma optical emission spectrometer (ICP-OES, Perkin Elmer, USA). The morphology of the catalyst and support was studied by Zeiss sigma 500/VP Scanning Electron Microscope (SEM). The morphological analysis and elemental distribution were carried out using Transmission Electron Microscopy (TEM, Jem 2100 F) with an acceleration voltage of 200 KV. Surface area measurements were performed with N$_2$ adsorption/desorption isotherms at 77 K (Micromeritics ASAP 2020 gas adsorption analyzer). Before the analysis, samples were outgassed at 200 °C for 4 h. Powder X-ray diffraction (XRD) was performed on a Bruker D8 Advance diffractometer using Cu Kα radiation generated at 40 kV and 40 mA. X-ray photoelectron spectra (XPS) and Auger electron spectroscopy were made on a Thermal Fisher system (Thermo scientific, Escalab 250Xi) employing an Al Kα radiation source. The binding energies for each spectrum were calibrated with a C 1s spectrum of 284.6 eV.

The graphitization degree of the NC support, obtained at different calcination temperatures, was studied by RENISHAW inVia micro confocal Raman spectrometer. Gas Chromatography-Mass Spectrometer (GC-MS) was performed on Shimadzu QP2020 GC-MS. Electrochemical workstation (CHI-760E) was used for electrochemical test. The conversion rate of the reactant and the yield of the product were analyzed by high performance liquid chromatography (HPLC). Shimadzu LC-20AT
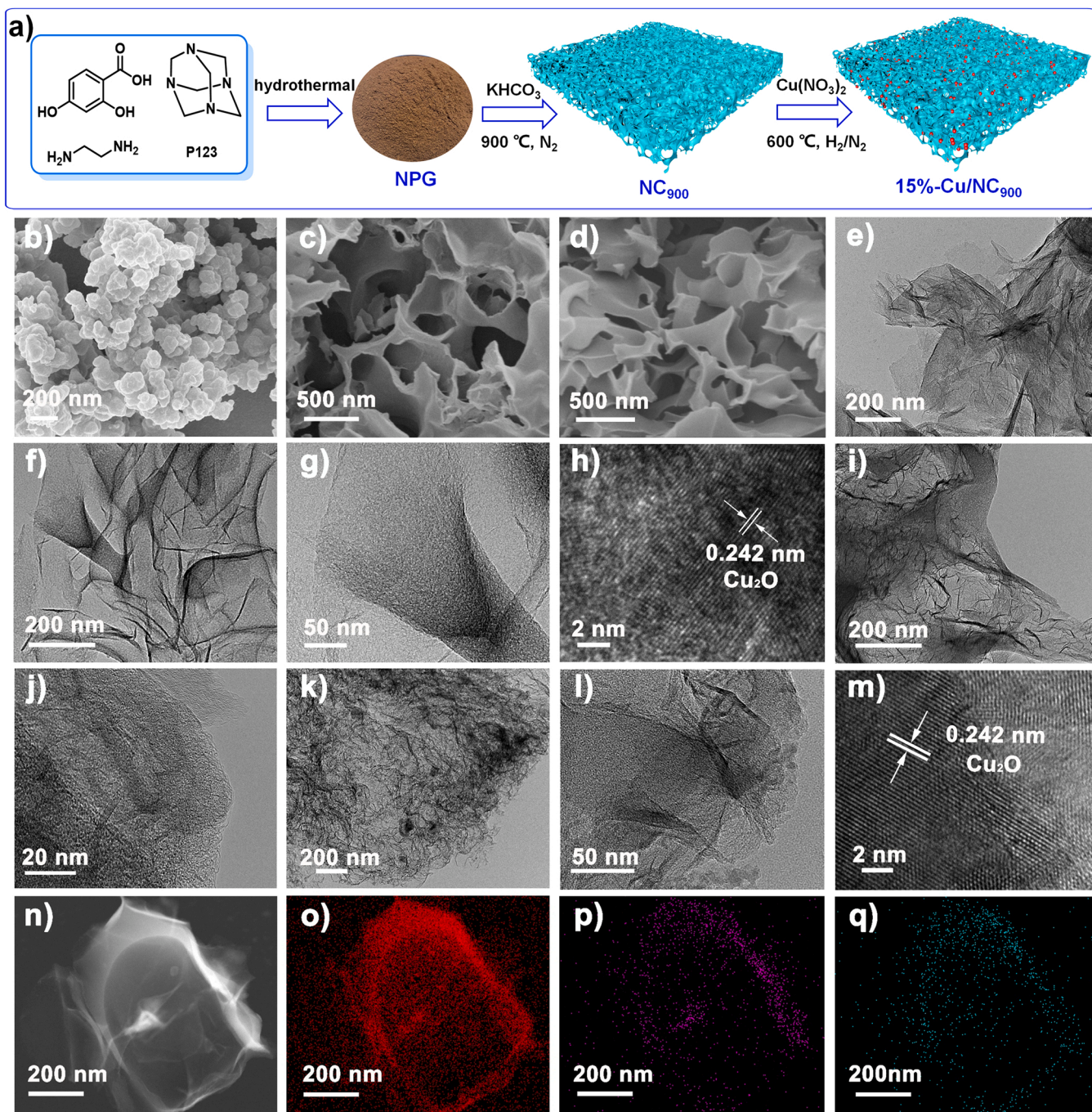
Fig. 2. (a) Schematic illustration for the preparation of 15%-Cu/NC$_{900}$. SEM images: (b) NPG, (c) NC$_{900}$ and (d) 15%-Cu/NC$_{900}$. TEM images: (e) NC$_{900}$, (f–h) 15%-Cu/NC$_{900}$, (i–j) 5%-Cu/NC$_{900}$, and (k–m) 25%-Cu/NC$_{900}$. (n) TEM-EDX mapping of 15%-Cu/NC$_{900}$, and the resulting elemental mapping of (o) C, (p) N, and (q) Cu presented in the 15%-Cu/NC$_{900}$.

were used for HPLC analysis by using InertSustain C18 column equipped with SPD-20A UV-Vis detector at 212 nm. A methanol-water (55:45 V/V) solution was used as the mobile phase at a flow rate of 0.8 mL min^{-1}.

2.5. Product analysis and calculations

In order to quantitatively calculate the yield of FA and the Faradaic efficiency of the reaction, a certain amount of reaction solution was taken after the reaction. After filtration, the reaction mixtures were quantitatively analyzed by HPLC.

The FF conversion (%) and FA yield (%) are calculated by the following equation:

$$Conversion\ (\%) = \frac{mole\ of\ substrate\ consumed}{mole\ of\ initial\ substrate} \times 100\%$$

$$Yield\ (\%) = \frac{mole\ of\ product\ formed}{mole\ of\ initial\ substrate} \times 100\%$$

The formula for calculating the Faradaic efficiency (FE) of the formed FA is as following:

$$FE(\%) = \frac{mole\ of\ product\ formed}{total\ charge\ passed/(n \times F)}$$

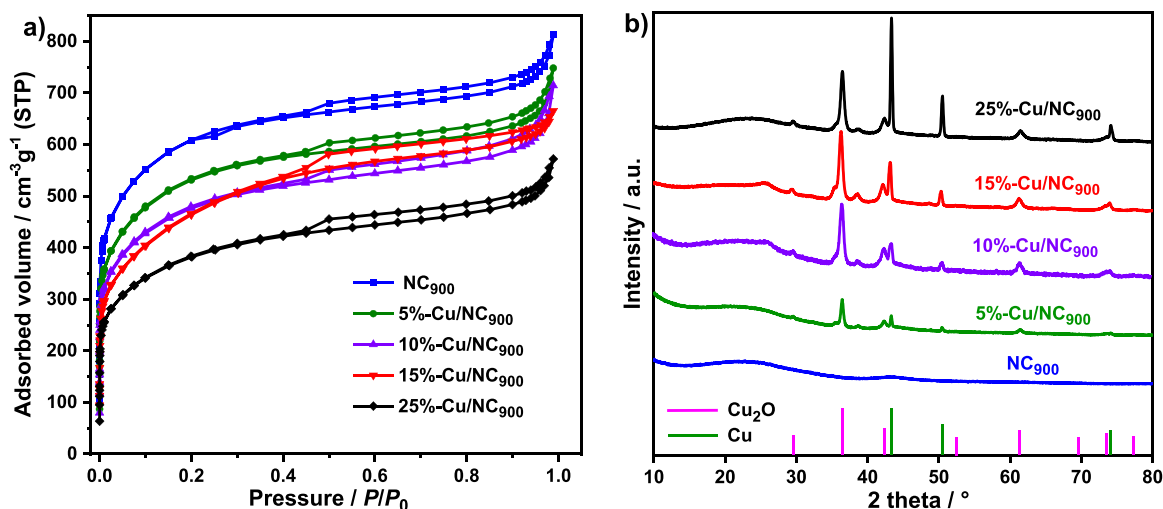Where n is the electron transfer number of each product and F is the

Fig. 3. NC_{900} and Cu/NC_{900} serial samples: (a) N_2 adsorption-desorption isotherms, (b) XRD patterns.

Faraday constant (96485 C mol^{-1}).

3. Results and discussion

3.1. Preparation and characterization of electrocatalyst

Herein, the 15%-Cu/NC$_{900}$ electrocatalyst with Cu mass-content of 15 wt% was obtained by initially impregnating NC$_{900}$ with Cu(NO$_3$)$_2$ and then pyrolyzing the obtained mixture at 600 °C under atmospheric H$_2$/N$_2$ (Fig. 2a). While, NC$_{900}$ was prepared by calcinating a mixture of nitrogen-containing polymer gel (NPG, Fig. 2a) and potassium bicarbonate (KHCO$_3$) at 900 °C according to our previous report [64]. The subscribe 900 in NC$_{900}$ denotes the final calcination temperature for the NC$_{900}$ preparation. The NPG was prepared by hydrothermal treatment a mixture of 2,4-dihydroxybenzoic acid, hexamethylentetramine, ethylenediamine and triblock copolymer (Pluronic P123). The as-prepared NC$_{900}$ support and the Cu/NC$_{900}$ catalysts with various Cu content were then systematically characterized.

Initially, the architecture of the obtained samples was analyzed by scanning electron microscopy (SEM). NPG exhibits irregular shapes (Fig. 2b). The SEM images of the resulting NC$_{900}$ show a three-dimensional (3D) morphology assembled by highly cross-linked and ultrathin N-doped carbon nanosheets (Fig. 2c). The transmission electron microscopy (TEM) analysis of NC$_{900}$ further confirms the wrinkled, rippled and crumpled nanosheet morphology (Fig. 2e). After loading Cu, the architecture of the resulting 15%-Cu/NC$_{900}$ is similar to NC$_{900}$ based

on the SEM (Fig. 2d) and TEM analyses (Fig. 2f–g). The interconnected 3D pore structure of 15%-Cu/NC$_{900}$ should have a great contribution to its surface area, mass diffusion and charge transfer during electrocatalytic process. Notably, highly dispersed Cu nanoparticles with uniform size on the 15%-Cu/NC$_{900}$ surface can only be observed with the high-resolution TEM (HRTEM). The detected 0.242 nm lattice fringes correspond to the (111) lattice plane of Cu$_2$O (Fig. 2h). In addition, the TEM energy dispersive X-ray (EDX) analysis further suggests a homogeneously dispersed Cu species throughout the 15%-Cu/NC$_{900}$ surface (Fig. 2n–q). Therefore, the TEM characterization of 15%-Cu/NC$_{900}$ suggests the presence of Cu(I) species on the 15%-Cu/NC$_{900}$ surface. Generally, 5%-Cu/NC$_{900}$ (Fig. 2i–j) and 25%-Cu/NC$_{900}$ (Fig. 2k–m) exhibit same architecture and lattice fringes of Cu with the 15%-Cu/NC$_{900}$.

The N$_2$ adsorption/desorption isotherm of NC$_{900}$ shows a steep increase at low P/P_0, which indicates the existence of abundant and rich micropores (Fig. 3a). Moreover, the presence of an evident hysteresis loop in a wide P/P_0 range confirms its mesoporous nature. Therefore, NC$_{900}$ exhibits micropore-prevailing hierarchically micro-mesoporous morphology with specific Brunauer−Emmet−Teller (BET) surface area of 2201 m^2 g^{-1} (Table 1). Upon Cu loading, the obtained Cu/NC$_{900}$ shows a significantly decreased specific surface area with increased Cu content. For example, the specific surface area is 1914 m^2 g^{-1} for 5%-Cu/NC$_{900}$, which remarkably reduces to 1369 m^2 g^{-1} for 25%-Cu/NC$_{900}$ (Table 1). Notably, all Cu/NC$_{900}$ samples keep hierarchically micro/mesoporous structure with micropore as prevailing architecture based

Table 1
Porosity properties of NC$_{900}$ and Cu/NC$_{900}$.

Sample	S_{BET}[a] (m^2 g^{-1})	S_{micro}[b] (m^2 g^{-1})	S_{ext}[c] (m^2 g^{-1})	D_{micro}[d]/D_{meso}[e] (nm)	V_{total}[f] (cm^3 g^{-1})	V_{micro}[g] (cm^3 g^{-1})	$V_{meso+macro}$[h] (cm^3 g^{-1})
NC$_{900}$	2201	1787	414	1.12/3.79	1.26	0.76	0.50
5%-Cu/NC$_{900}$	1914	1600	314	1.12/3.79	1.16	0.70	0.46
10%-Cu/NC$_{900}$	1715	1387	328	1.12/3.79	1.11	0.61	0.50
15%-Cu/NC$_{900}$	1641	1250	391	1.34/3.79	1.03	0.59	0.44
25%-Cu/NC$_{900}$	1369	1065	304	1.12/3.79	0.88	0.47	0.41
15%-Cu$^{(II)}$/NC$_{900}$	1275	1035	240	1.41/3.79	0.86	0.45	0.41

[a] S_{BET}, BET surface area.
[b] S_{micro}, BET surface area of micropores.
[c] S_{ext}, external surface area.
[d] D_{micro}, micropore diameter.
[e] D_{meso}, mesopore diameter.
[f] V_{total}, total pore volume.
[g] V_{micro}, pore volume of micropore.
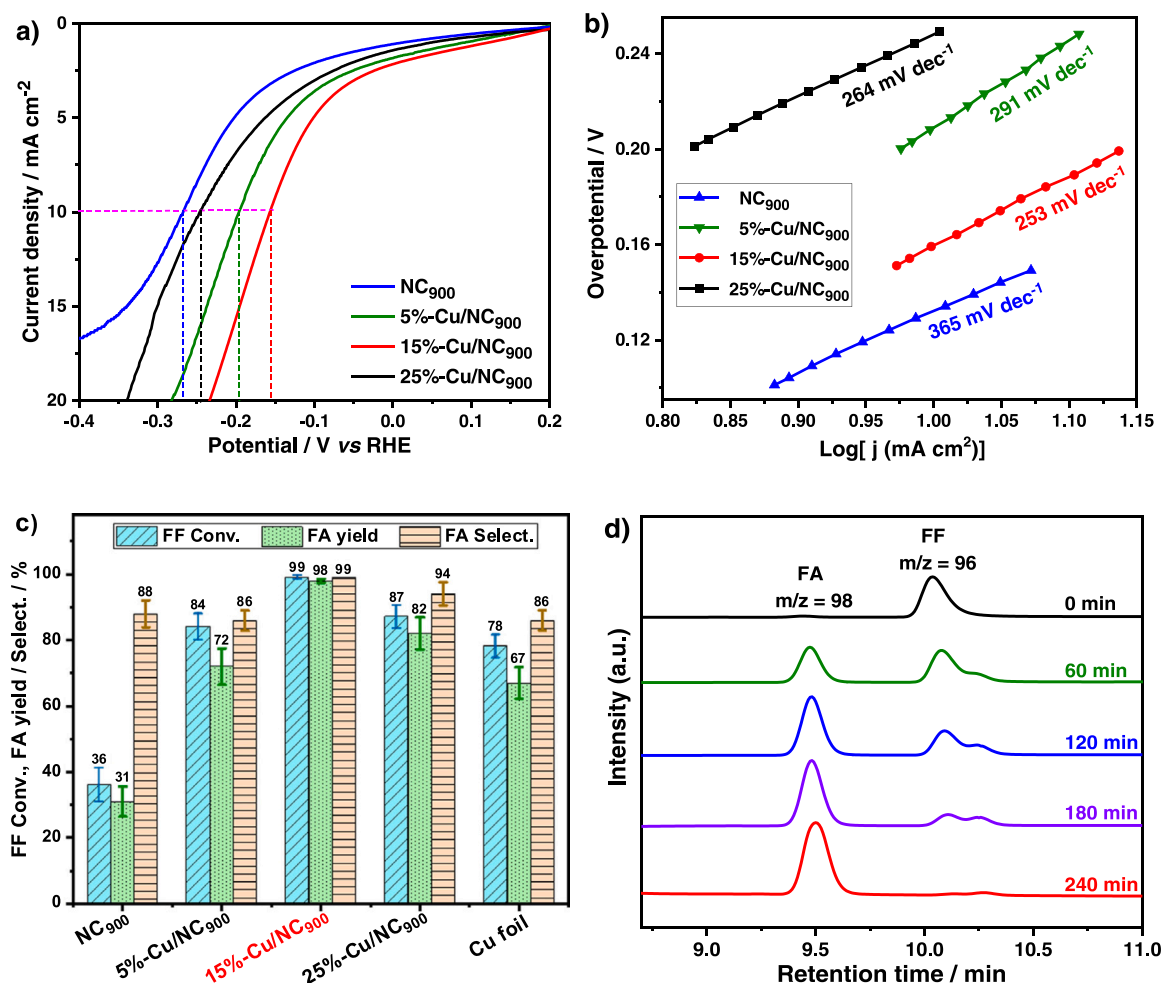[h] $V_{meso+macro}$, pore volume of mesopore and macropore.

Fig. 4. NC$_{900}$ and Cu/NC$_{900}$ serial catalysts for ECH of FF: (a) LSV, (b) the corresponding Tafel slope, and (c) effect of Cu loading level on the electrocatalytic performance. (d) Time-dependent HPLC analysis of 15%-Cu/NC$_{900}$-promoted ECH of FF. Reaction conditions: (a) electrolyte (aqueous solution of 1.0 M KOH), FF (30 mM in aqueous media), scan rate (100 mV s^{-1}); (c and d) applied voltage (−1.3 V) and electrolysis time (240 min) was used.

on the analysis from N$_2$ sorption isotherm (Fig. 3a) and pore size distribution (Fig. S5e, Supporting Information).

Both NC$_{900}$ and Cu/NC$_{900}$ were further analyzed with X-ray diffraction (XRD). For NC$_{900}$, a broad diffraction peak at 25.0° was observed (Fig. 3b), corresponding to amorphous carbon. In the case of Cu/NC$_{900}$ with various Cu contents, their characteristic peaks are similar with each other, which proves the presence of same components in these samples. In addition to the evident diffraction peak arisen from amorphous carbon, Cu/NC$_{900}$ samples with different Cu contents exhibit three characteristic peaks at 43.3°, 50.4° and 74.3°, respectively, corresponding to the plane reflections of (111), (200) and (220) crystal planes from metallic copper (JCPDF file No. 04-0836). Moreover, another three typical peaks at 36.5°, 42.3° and 61.3° were observed with Cu/NC$_{900}$ serial samples, which can be respectively assigned to crystal plane reflections from (111), (200), and (220) of Cu$_2$O (JCPDF file No. 05-0667). In addition, as expected, the intensities of both Cu(0) and Cu (I) phases in the Cu/NC$_{900}$ serial samples enhanced with their Cu content (5–25%). Generally, the XRD result of Cu/NC$_{900}$ samples is consistent with their analysis from HRTEM, indicating the main component of Cu$_2$O in all Cu/NC$_{900}$ samples. Our XRD characterization thus demonstrates successful reduction of Cu(II) precursor to Cu(I) and Cu(0) species during pyrolysis treatment under atmospheric H$_2$/N$_2$ to give Cu/NC$_{900}$.

3.2. Evaluation ECH of furfural with Cu catalyst

After systematic characterization, the obtained Cu/NC$_{900}$ samples were made into catalyst-inks and then dripped onto 1.0 × 1.0 cm^2 carbon cloth for the preparation of working electrodes. These electrodes were subsequently investigated for FF-to-FA transformation via ECH in aqueous media in an H-type electrolyzer at ambient temperature (Figs. 1 and S1, Supporting Information). Aqueous KOH solution (1.0 M) was selected as electrolyte with FF concentration of 30 mM for the electrolysis. Atmospheric N$_2$ was initially bubbled into the reaction mixture for 0.5 h before the electrolysis. After the reaction, the obtained reaction solution was filtered and diluted with water for high performance liquid chromatography (HPLC) analysis. FF conversion, FA yield and FA selectivity were obtained by their corresponding concentrations based on the HPLC analysis. Notably, Cannizzaro disproportionation reaction of FF to furoic acid and FA was unobserved under the investigated conditions. Generally, high concentrations of both KOH solution (18 M) and FF (5 M) are required to push the Cannizzaro reaction at an elevated reaction temperature (60 °C) [65–67]. In our case, the concentrations of KOH (1 M) and FF (30 mM) are very low; moreover, the ECH of FF to FA is performed at ambient temperature.

Initially, the effect of Cu content in Cu/NC$_{900}$ on its electrocatalytic performance was probed. The Cu/NC$_{900}$ with various Cu loading levels were respectively loaded onto the carbon cloth and subsequently evaluated for the ECH of FF. We tested the linear scan voltammogram (LSV) curves of various Cu/NC$_{900}$ (Fig. 4a). The electrode was initially
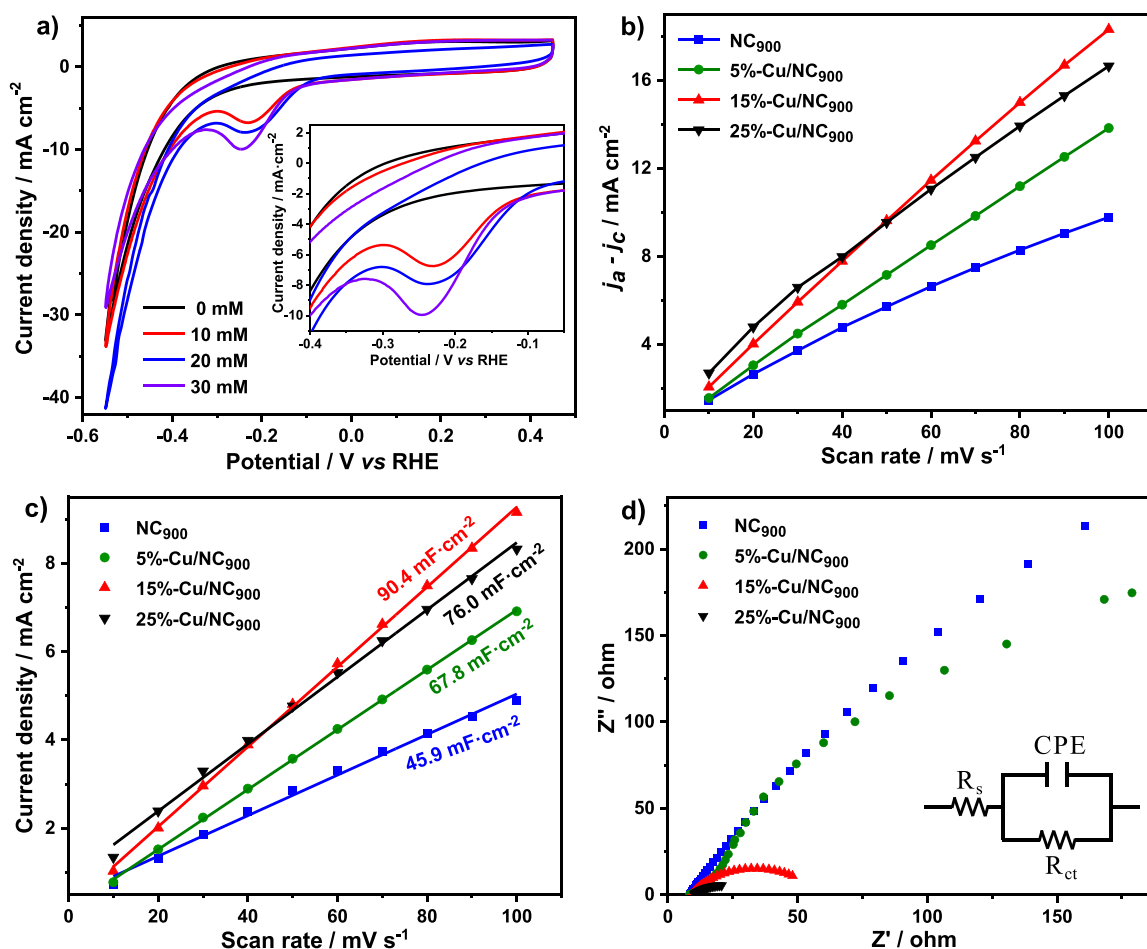
Fig. 5. (a) CV of 15%-Cu/NC$_{900}$ loaded on glassy carbon electrode for ECH of FF at various FF concentrations with the scan rate of 100 mV s^{-1}. NC$_{900}$ and Cu/NC$_{900}$ serial catalysts for ECH of FF: (b) current density difference (j_a−j_c) at various scanning rates, (c) double layer capacitance (C$_{dl}$) measured by CV, (d) electrochemical impedance spectrogram.

activated each time by 20 cycles of cyclic voltammetry (CV) with a scanning rate of 100 mV s^{-1} before the measurement. It was found that 15%-Cu/NC$_{900}$ exhibits a minimum overpotential (potential corresponding to current density of 10 mA cm^{-2}) of about 155 mV in aqueous solution of 30 mM FF. In sharp contrast, the pristine NC$_{900}$ support shows the largest over potential of 265 mV. These observations indicate that the Cu/NC$_{900}$ serial catalysts can effectively reduce the over potential for FF hydrogenation.

In order to investigate the competition between electrocatalytic hydrogen evolution and FF hydrogenation, the LSV curves of 15%-Cu/ NC$_{900}$ before and after FF addition were compared in Fig. S2a (Supporting Information). It was found that the overpotential of the system shifts positively from −1.47 to −1.31 V after FF addition, demonstrating a preferential reaction of FF hydrogenation over hydrogen evolution on the 15%-Cu/NC$_{900}$ surface. At the same time, no bubbles were observed on the surface of carbon cloth after FF addition, which further confirms a prior reaction of FF hydrogenation on the 15%-Cu/NC$_{900}$ surface. The Tafel slope was then obtained by fitting the corresponding LSV curve (Fig. 4b). As a result, 15%-Cu/NC$_{900}$ has the smallest Tafel slope of 253 mV dec^{-1}. According to the results of LSV and Tafel slope, we thus speculate that 15%-Cu/NC$_{900}$ should have the best electrocatalytic performance for ECH of FF.

The ECH activity of Cu/NC$_{900}$ serial catalysts was then compared by FF-to-FA transformation with constant potential electrolysis. As expected, the loading of Cu on the NC$_{900}$ support can significantly enhance the electrocatalytic activity of the resulting Cu/NC$_{900}$ samples (Fig. 4c). Moreover, 15%-Cu/NC$_{900}$ shows the highest ECH performance by

producing FA yield of 98% with FF conversion of 99% (Fig. 4c). Our time-dependent HPLC analysis clearly demonstrated a decreased FF concentration with an increasing concentration of FA (Fig. 4d). Moreover, FA was detected as a final product with full conversion of FF at the ECH time of 240 min. In contrast, 5%-Cu/NC$_{900}$ gives only 72% yield of FA under the investigated conditions (Fig. 4c), due to the lack of active sites at a low loading level of Cu. The reduced catalytic activity of 5%-Cu/NC$_{900}$ can also be related to its low ECSA (1695 cm^2, Table S1, Supporting Information). In sharp contrast, a significantly increased ECSA to 2261 cm^2 is observed with 15%-Cu/NC$_{900}$ (Table S1). While, a significantly increased Cu content to 25%-Cu/NC$_{900}$, again, leads to a reduced FA yield to 82%. This observation can be attributed to pore blockage in the 25%-Cu/NC$_{900}$ by a significantly increased Cu nanoparticle size, resulting in an insufficient mass-transfer and the exposure of the active sites. This assumption can be supported by our analysis from N$_2$ adsorption/desorption isotherm. The BET surface area for 25%-Cu/NC$_{900}$ is 1369 m^2 g^{-1} (Table 1); while, an increased surface area to 1641 m^2 g^{-1} is obtained from 15%-Cu/NC$_{900}$. Moreover, the ECSA is 1900 cm^2 for 25%-Cu/NC$_{900}$, which is, again, low than that of 15%-Cu/ NC$_{900}$. Therefore, the high activity of 15%-Cu/NC$_{900}$ over 5%-Cu/NC$_{900}$ and 25%-Cu/NC$_{900}$ can be attributed to their ECSA and surface area. Finally, commercially available Cu foil electrode (1.0 × 1.0 cm^2) was performed with the electrolysis experiment for comparison purpose under the investigated conditions, giving 67% yield of FA with FF conversion of 78% (Fig. 4c). Therefore, our evaluation of ECH performance for Cu/NC$_{900}$ serial catalysts suggests excellent activity of 15%-Cu/NC$_{900}$ over other samples.
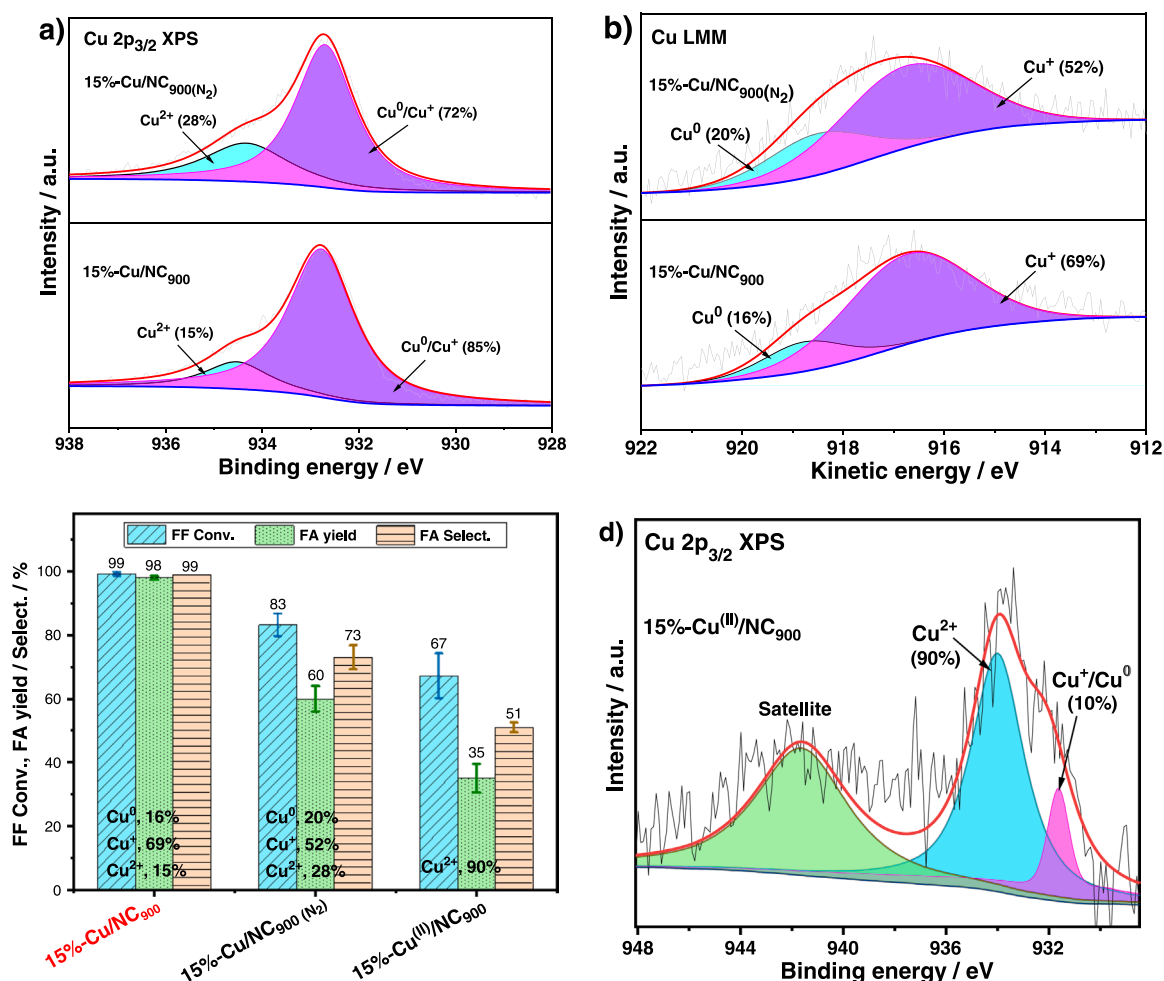
Fig. 6. 15%-Cu/NC$_{900}$ and 15%-Cu/NC$_{900(N2)}$: (a) Cu 2p$_{3/2}$ XPS and (b) Cu LMM. (c) Effect of surface-Cu valence state on the ECH activity of 15%-Cu/NC$_{900}$. (d) Cu 2p$_{3/2}$ XPS of 15%-Cu$^{(II)}$/NC$_{900}$. Reaction conditions: (c) electrolyte (aqueous solution of 1.0 M KOH), FF (30 mM in aqueous media), applied voltage (−1.3 V), electrolysis time (240 min).

The electrochemical behavior of Cu/NC$_{900}$ serial catalysts were further investigated by their loading on a glassy carbon disk electrode (diameter, 3 mm) for electrochemical measurement. 15%-Cu/NC$_{900}$ was initially examined as electrocatalyst to obtain CV curves with various FF concentrations at the scanning rate of 100 mV s^{-1} (Fig. 5a). Only an irreversible reduction peak at −0.25 V (*vs.* RHE, Reversible Hydrogen Electrode) was detected in the CV curve, corresponding to electro-reduction of FF to FA on the 15%-Cu/NC$_{900}$ surface.

It has been reported that the growth rate of HER kinetics is faster than that of FF/5-hydroxymethylfurfural (HMF)-reduction kinetics at high overpotential [58,68]. In our case, this result can be further confirmed by the comparison of LSV curves before and after FF addition (Fig. S2b). When FF was added for ECH, the initial potential was only 40 mV positive shift; while, the overpotential was 170 mV positive shift compared to HER. Therefore, there was no significant difference in the initial potential between FF hydrogenation and HER. In other words, the addition of FF does not affect the formation of H$_{ads}$ in the Volmer reaction (reaction R1), which is essential to the efficient electrocatalyst for FF hydrogenation. However, there is an over-potential difference of 170 mV between FF hydrogenation and HER. Therefore, H$_2$ generation from H$_{ads}$ by Heyrovsk (reaction R2) or Tafel (reaction R3) processes was successfully inhibited. Meanwhile, these active and adsorbed H$_{ads}$ species on the electrocatalyst surface can selectively react with FF to produce FA. However, the overpotential shifts negatively when FF hydrogenation is finished, and HER process can subsequently proceed again (Fig. S2b).

The ECSA of NC$_{900}$ and Cu/NC$_{900}$ serial catalysts were then evaluated with a regular voltage window from 0.1 to 0.2 V (*vs.* RHE) for the CV curves at the scan rate range of 10 ~ 100 mV s^{-1}. The CV curves of NC$_{900}$ and Cu/NC$_{900}$ catalysts show typical rectangles, which are characteristic of carbon materials (Fig. S3, Supporting Information). Fig. 5b shows the resulting curve of $j_a - j_c$ *vs* scanning rate, a subsequent fitting of Fig. 5b gives the plots of current density *vs* scanning rate (Fig. 5c) with all correlation coefficients greater than 0.99 (Table S1). The resulting ECSA are 1148 cm^2 for NC$_{900}$, 1695 cm^2 for 5%-Cu/NC$_{900}$, 2261 cm^2 for 15%-Cu/NC$_{900}$ and 1990 cm^2 for 25%-Cu/NC$_{900}$, respectively. Obviously, 15%-Cu/NC$_{900}$ shows the highest ECSA value and, in principle, should have the highest activity in the ECH process among various investigated Cu catalysts, which has been confirmed by our experimental results (Fig. 4c).

Electrochemical impedance often demonstrates the electron transfer efficiency of the investigated catalyst. Generally, the smaller the circle radius is in the Nyquist diagram, the better electron transfer speed is suggested for the investigated catalyst, thus indicating a positive contribution of the catalyst to the redox process. As shown in Fig. 5d, both 15%-Cu/NC$_{900}$ and 25%-Cu/NC$_{900}$ show smaller arc radius among the investigated samples, which demonstrates a quick electron transfer on their surfaces. In fact, 25%-Cu/NC$_{900}$ exhibits the smallest electrochemical impedance due to its relatively high Cu content. Our ECH experiments of FF-to-FA transformation has demonstrated a superior activity of 15%-Cu/NC$_{900}$ over 25%-Cu/NC$_{900}$ (Fig. 4c).
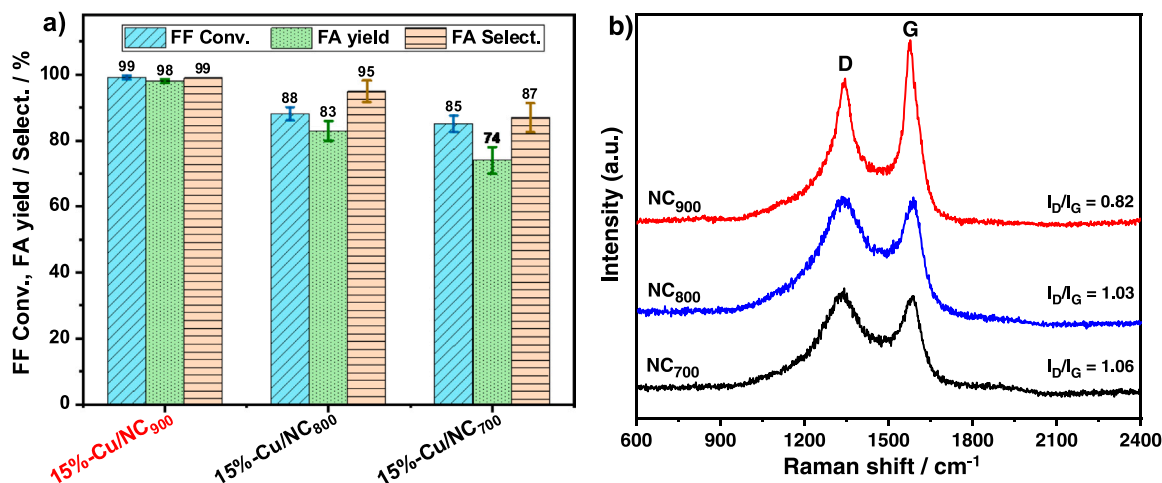
Fig. 7. (a) Effect of NC-calcination temperature on the electrocatalytic performance of 15%-Cu/NC serial samples. (b) Raman spectra of NC serial samples. Reaction conditions: (a) electrolyte (aqueous solution of 1.0 M KOH), FF (30 mM in aqueous media), applied voltage (−1.3 V), electrolysis time (240 min).

3.3. Effect on surface-Cu valence on the ECH

The influence of surface-Cu valence state on the ECH activity of 15%-Cu/NC$_{900}$ was then investigated. 15%-Cu/NC$_{900}$ was obtained by pyrolyzing NC$_{900}$-supported melamine-Cu(NO$_3$)$_2$ at 600 °C under atmospheric H$_2$/N$_2$. The 15%-Cu/NC$_{900}$ was performed with X-ray photoelectron spectroscopy (XPS) characterization to probe its surface elemental composition as well as chemical state. Four elements including C, N, O and Cu were detected as shown in XPS scan survey of 15%-Cu/NC$_{900}$ (Fig. S4a, Supporting Information). The Cu 2p$_{3/2}$ XPS of 15%-Cu/NC$_{900}$ exhibits two characteristic peaks at 934.3 and 932.7 eV, respectively corresponding to Cu^{2+} and Cu$^+$/Cu^0 species (Fig. 6a). Since Cu$^+$ and Cu^0 cannot be distinguished by Cu 2p XPS, Cu LMM Auger spectra of 15%-Cu/NC$_{900}$ were then fitted (Fig. 6b), showing two characteristic peaks at 916.6 eV (assigned to Cu$^+$) and 918.4 eV (indexed to Cu^0). The integration areas of these Cu species, appeared in Cu LMM Auger spectra (Fig. 6b) and Cu 2p$_{3/2}$ XPS (Fig. 6a), indicates Cu$^+$ (69%) as a prevailing species over Cu^0 (16%) and Cu^{2+} (15%) species. Finally, N 1s XPS of 15%-Cu/NC$_{900}$ shows three main peaks at 398.2 eV (pyridinic N), 400.2 eV (graphitic N) and 403.5 eV (pyridine *N*-oxide) with graphitic N as the predominant species (Fig. S4b).

Therefore, the 15%-Cu/NC$_{900}$, obtained under H$_2$/N$_2$, exhibits a mixed valence state of Cu, which includes Cu^{2+} (15%), Cu$^+$ (69%) and Cu^0 (16%) with Cu(I) as the predominant species. When 15%-Cu/NC$_{900}$ was prepared by calcinating NC$_{900}$-supported melamine-Cu(NO$_3$)$_2$ under atmospheric N$_2$, the resulting 15%-Cu/NC$_{900(N2)}$ sample shows almost the same XPS results with 15%-Cu/NC$_{900}$ (Fig. 6a and b). However, the 15%-Cu/NC$_{900(N2)}$ exhibits an enhanced content of Cu^{2+} (28%) species with reduced percentages of Cu$^+$ (52%) and Cu^0 (20%) species on the sample surface when compared with those of 15%-Cu/NC$_{900}$. The difference of Cu-valence states in 15%-Cu/NC$_{900}$ and 15%-Cu/NC$_{900(N2)}$ can also be observed in XRD patterns (Fig. S5b, Supporting Information). Under such conditions, the observed Cu$^+$ and Cu^0 species on the 15%-Cu/NC$_{900(N2)}$ surface are presumably attributed to Cu(NO$_3$)$_2$-reduction with melamine by releasing H$_2$O and ammonia during the carbothermal process under the N$_2$ atmosphere. Notably, 15%-Cu/NC$_{900(N2)}$ displays a significantly reduced FA yield to 60% when compared with 98% yield of FA from 15%-Cu/NC$_{900}$ under the investigated conditions (Fig. 6c). Therefore, the oxidation state of surface Cu species on the 15%-Cu/NC$_{900}$ should play an important role on its ECH performance.

To further probe the valence state of Cu on the electrocatalytic activity of 15%-Cu/NC$_{900}$, the 15%-Cu/NC$_{900}$ with predominant CuO species on the surface [denoted as 15%-Cu$^{(II)}$/NC$_{900}$] was prepared by hydrolysis of copper (II) acetylacetonate [Cu(acac)$_2$] in methanol in the existence of NC$_{900}$ under supercritical carbon dioxide (*sc*-CO$_2$) conditions. The resulting 15%-Cu$^{(II)}$/NC$_{900}$ shows a high specific BET surface area of 1275 m^2 g^{-1} (Table 1, Fig. S5a) with similar morphology to 15%-Cu/NC$_{900}$ according to TEM analysis (Fig. S5c). However, the observed Cu lattice spacing of 15%-Cu$^{(II)}$/NC$_{900}$ is 0.277 nm, corresponding to a typical CuO(110) crystal face (Fig. S5d). Moreover, the diffraction peaks corresponding to the crystalline phases of Cu were unobserved (Fig. S5b), presumably due to its poor Cu crystalline phase formed under the *sc*-CO$_2$ conditions. The oxidation state of surface Cu for 15%-Cu$^{(II)}$/NC$_{900}$ was further investigated by XPS analysis as shown in Fig. 6d. The Cu 2p$_{3/2}$ XPS of 15%-Cu$^{(II)}$/NC$_{900}$ exhibits a characteristic peak at 934.3 eV, which can be assigned as Cu^{2+} (90%) species. However, the resulting Cu LMM Auger spectra of 15%-Cu$^{(II)}$/NC$_{900}$ fail to elucidate Cu(I) and Cu(0) species because of their low abundances on the sample surface. Therefore, our TEM, XRD and XPS analyses confirm a prevailing Cu^{2+} (90%) species on the 15%-Cu$^{(II)}$/NC$_{900}$ surface, which is significantly different from a predominant Cu$^+$ (69%) species on the 15%-Cu/NC$_{900}$ surface. However, the obtained 15%-Cu$^{(II)}$/NC$_{900}$ shows remarkably reduced FA yield to 35% with significantly low selectivity of 51% when compared with a 98% yield of FA from 15%-Cu/NC$_{900}$ (Fig. 6c). Therefore, 15%-Cu/NC$_{900}$ shows a superior electrocatalytic performance over other Cu catalysts and Cu foil electrode, the surface Cu (I)/Cu(0) species are presumably true active sites for ECH of FF to FA.

3.4. Effect of catalyst support on the ECH

Catalyst support plays an important role on the electrocatalytic performance of its resulting catalyst. In our case, the NC support was obtained by calcinating a mixture of NPG and KHCO$_3$ under N$_2$ atmosphere. Therefore, the influence of NC-calcination temperature on the electrocatalytic performance of the resulting 15%-Cu/NC was finally explored. As shown in Fig. 7a, the 15%-Cu/NC$_{900}$ obtained by NC-calcination at 900 °C evidently shows high ECH performance over its analogs such as 15%-Cu/NC$_{800}$ and 15%-Cu/NC$_{700}$. Under such conditions, NC$_{800}$ and NC$_{700}$ were respectively prepared by NC-calcination at 800 °C and 700 °C. This result can presumably be related to the influence of calcination temperature on graphitization degree of the resulting NC support. The Raman spectroscopy of NC$_{900}$ exhibits two characteristic absorption peaks at 1350 and 1580 cm^{-1}, which respectively corresponds the D-band and G-band of carbon (Fig. 7b). The value of I$_D$/I$_G$ (the peak-intensity ratio of D-band to G-band) is 0.82 for NC$_{900}$, which is much lower than 1.03 for NC$_{800}$ and 1.06 for NC$_{700}$. A higher graphitization degree of NC$_{900}$ can presumably lead to a quick electron transfer, thus contribute to an enhanced electrocatalytic performance of the obtained 15%-Cu/NC$_{900}$.
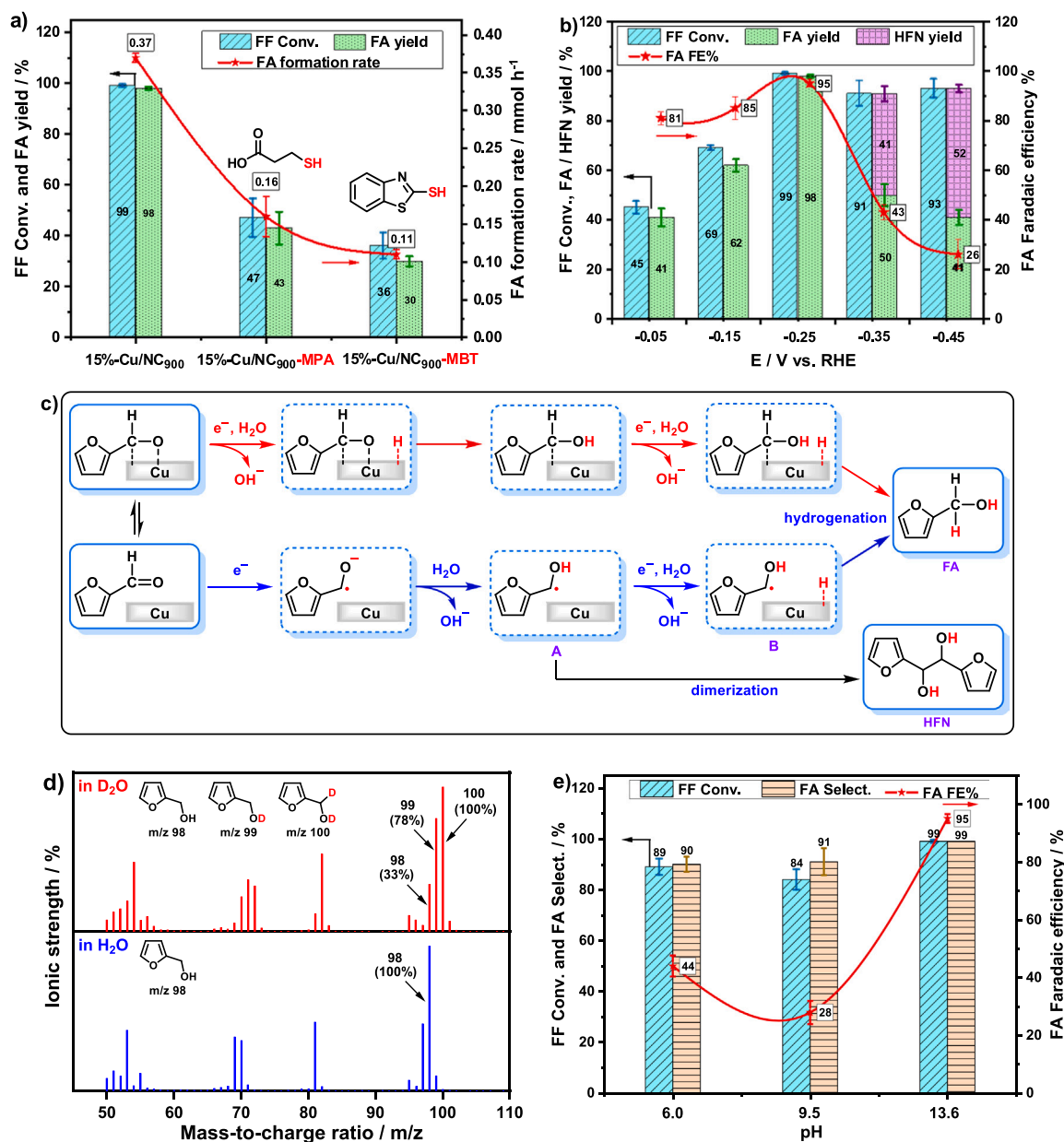
Fig. 8. (a) Observed formation rate of FA during preparative electrolysis of FF on 15%-Cu/NC$_{900}$, 15%-Cu/NC$_{900}$-MPA, and 15%-Cu/NC$_{900}$-MBT electrodes. (b) FF conversion, FA/HFN yields and Faradaic efficiency at various potentials using 15%-Cu/NC$_{900}$ electrode. (c) Proposed mechanism for FF transformation into FA and HFN over 15%-Cu/NC$_{900}$ in H$_2$O/NaOH electrolyte. (d) Mass spectra of FA obtained from D$_2$O/NaOH and H$_2$O/NaOH. (e) ECH of FF to FA over 15%-Cu/NC$_{900}$ at various pH levels. Reaction conditions: (a) electrolyte (aqueous solution of 1.0 M KOH), FF (30 mM in aqueous media), organothiol (0.5 mM), applied voltage (−1.3 V), electrolysis time (240 min); (b) electrolyte (aqueous solution of 1.0 M KOH), FF (30 mM in aqueous media), electrolysis time (240 min); (d) electrolyte (1.0 M KOH in D$_2$O and H$_2$O), FF (30 mM in D$_2$O and H$_2$O), applied voltage (−1.3 V), electrolysis time (240 min). (e) FF (30 mM), applied voltage (−1.3 V), pH 6.0 (0.5 M K$_2$SO$_4$), pH 9.5 (0.5 M K$_2$B$_4$O$_7$), pH 13.6 (1.0 M KOH).

3.5. Mechanism investigation

Previous research demonstrated two distinct mechanisms for FF hydrogenation over metallic Cu electrode, which includes ECH and direct electroreduction [32,39]. The detected distributions of product and by-product were closely related to the contributions from each mechanism. In our case, electrode processes were initially probed to understand the mechanism of the FF hydrogenation over 15%-Cu/NC$_{900}$. The 15%-Cu/NC$_{900}$ electrode was respectively modified with self-assembled monolayers (SAMs) of organothiols involving 3-mercaptopropionic acid (MPA) and mercaptobenzothiazole (MBT). The obtained MPA-modified 15%-Cu/NC$_{900}$ (denoted as 15%-Cu/NC$_{900}$-MPA) and MBT-modified 15%-Cu/NC$_{900}$ (denoted as 15%-Cu/NC$_{900}$-MBT) were compared with the pristine 15%-Cu/NC$_{900}$ by constant-potential preparative electrolysis of FF in aqueous KOH electrolyte with pH of 13.6. As shown in. Fig. 8a, the formation rates of FA were significantly suppressed over thiol-modified electrodes. For instance, the FA formation rate decreased from 0.37 mmol$_{FA}$ h^{-1} for pristine 15%-Cu/NC$_{900}$ to 0.16 mmol h^{-1} for 15%-Cu/NC$_{900}$-MPA, and further reduced to 0.11 mmol h^{-1} for 15%-Cu/NC$_{900}$-MBT under the investigated conditions (Fig. 8a). The conjugated molecular structure of MBT should more effectively block active surface sites and thus inhibit inner-sphere electron transfer (ET) if compared with MPA. This result indicates that hydrogenation pathways to FA require direct interactions of reactants with the electrode surface of 15%-Cu/NC$_{900}$ via ECH mechanism as shown in Fig. 8c (red and blue routes). In the case of direct
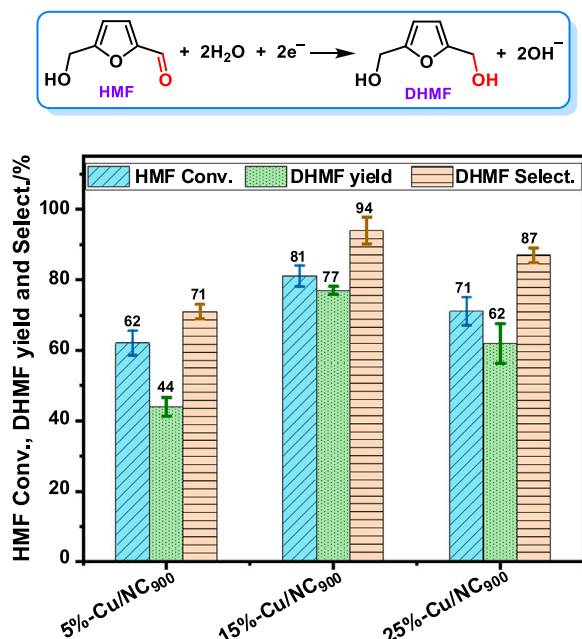
Fig. 9. ECH of HMF with Cu/NC$_{900}$ serial catalysts. Reaction conditions: electrolyte (aqueous solution of 1.0 M KOH), HMF (30 mM in aqueous media), applied voltage (−1.3 V) and electrolysis time (240 min).

electroreduction mechanism, FF reduction is expected to be unaffected by such SAM-modifications because it occurs mainly through an outer-sphere ET process and does not need initial and specific adsorption of H or FF [32].

To probe the dependence of product distribution on the potential, the ECH was then performed at various fixed potentials from −0.05 to −0.45 V (vs. RHE) for 4 h by using 15%-Cu/NC$_{900}$ (Fig. 8b). Initially, both FF conversion (45%) and FA yield (41%) were moderate at −0.05 V with the corresponding Faradaic efficiency of 81% to FA. Then, both FA yield and FF conversion enhanced when more negative voltage was applied to the working electrode within the potential range from −0.05 to −0.25 V, achieving over 98% yield of FA with 95% Faradaic efficiency at −0.25 V. Nevertheless, further increased potentials from −0.35 to −0.45 V led to a significantly reduced FA yield and faradaic efficiency due to HFN formation and H$_2$ evolution (Fig. 8b and S6, Supporting Information). Typically, a 52% yield of FA was observed at −0.45 V with the Faradaic efficiency only 26%. Evidently, low potential (from −0.05 to −0.25 V) predominantly promotes the ECH path way for FA formation, presumably due to low and well-matched concentrations between H$_{ads}$ and FA radical over 15%-Cu/NC$_{900}$ surface (**B**, Fig. 8c). Under such conditions, HFN was unobserved to any detectable extents. In contrast, ECH and reductive dimerization competitively performed at high potential (from −0.35 to −0.45 V), which can be attributed to high formation rate of FA radical (**A**, Fig. 8c), leading to its enhanced adsorption on the Cu surface. Finally, the accumulation of FA radical facilitated its dimerization to yield HFN (black route, Fig. 8c). Therefore, the proposed ECH mechanism for FF-to-FA transformation involved a second proton-coupled electron transfer with H$_{ads}$ formation as key species for the hydrogenation (red and blue routes, Fig. 8c). In contrast,
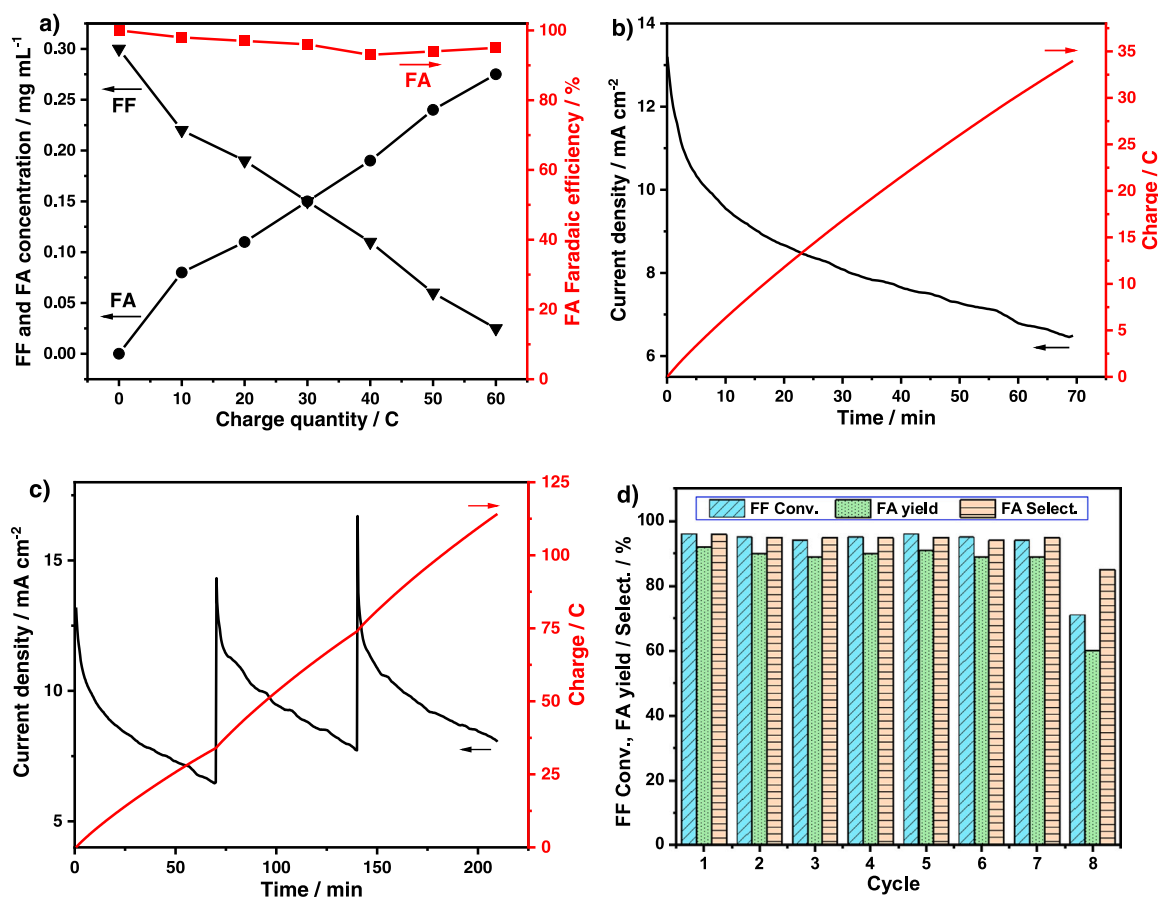

Fig. 10. ECH of FF to FA: (a) plots of FF/FA concentrations and Faradaic efficiency *vs* various amounts of passed charge in the electrolysis, (b) the charge and its corresponding current density *vs* reaction time in 1.0 M KOH containing 30 mM FF, (c) accumulated charge and its corresponding current density *vs* reaction time by successively adding fresh 30 mM FF in twice, (d) consecutive use of 15%-Cu/NC$_{900}$ electrode at −1.3 V potential in 1.0 M KOH containing 30 mM FF.

dimerization route of FA radical resulted in HFN product. The selectivities to FA and HFN in the ECH process is mainly controlled by the required potential for H_{ads} formation on the cathode.

Hydrogen source for ECH of FF was finally investigated by isotopic labeling study with 15%-Cu/NC$_{900}$. The ECH of FF was respectively performed with H$_2$O/KOH and D$_2$O/KOH electrolytes, the resulting products were analyzed by Gas Chromatography-Mass Spectrometer. Fig. 8d shows MS of the FA formed from FF−H$_2$O/KOH, the resulting FA exhibits the most abundant parent molecular ions at $m/z = 98$, demonstrating the formation of 2-furanylmethanol. In contrast, the FA, obtained from FF−D$_2$O/KOH, involved at least three compounds of 2-furanylmethanol ($m/z = 98$, 33%), 2-furanylmethanol-d ($m/z = 99$, 78%), and 2-furanylmethan-d-ol-d ($m/z = 100$, 100%) with the 2-furanylmethan-d-ol-d as the most prevailing molecule. Our isotopic labeling investigation thus unambiguously indicates that the hydrogen source was H$_2$O from the electrolyte for the ECH [63,69] (Fig. 8d).

Finally, the pH effect of electrolyte on the ECH of FF was investigated over 15%-Cu/NC$_{900}$ catalyst (Fig. 8e). Generally, the selectivities to FA were all above 90% with a broad pH value range from 6.0 to 13.6 for the electrolytes under the investigated condition; however, the corresponding faradaic efficiency were moderate to low (44–28%) at low pH values (6.0–9.5) of the electrolytes. In contrast, both selectivity and faradaic efficiency of FA exceeding 95% were observed under high pH value (13.6) of the electrolytes.

3.6. ECH of 5-hydroxymethylfurfural with Cu catalyst

Inspired by the above results, Cu/NC$_{900}$ serial catalysts were further applied to the ECH of biomass-based HMF to 2,5-dihydroxymethylfuran (DHMF) under the optimal conditions. Again, 15%-Cu/NC$_{900}$ shows the highest ECH performance by producing DHMF in 77% yield with selectivity of 94% (Fig. 9), thus demonstrating excellent selectivity of the Cu electrocatalyst for the ECH of C=O bond in HMF.

3.7. Catalyst stability and recyclability

The electrocatalytic efficiency and stability of 15%-Cu/NC$_{900}$ were then investigated with the ECH of FF to FA. Initially, every 10 Coulomb (C) of electric charges were input into the ECH system to calculate the FF conversion rate, FA yield and the resulting Faradaic efficiency (Fig. 10a). The concentration of FA proportionally increases with a decreased FF concentration; while, the resulting Faradaic efficiency for the FF-to-FA transformation is above 94% at 60 C with FA yield of 90%.

To further probe the correlation between current density/charge and electrolysis time during the ECH process, the ECH of FF was performed by electrolysis for 70 min at −0.25 V (*vs.* RHE) bias voltage (Fig. 10b). The observed results show a decreased current density and increased charge with electrolysis time. At the end of this process, another fresh 30 mM FF was directly added into the electrolytic cell, the resulting current density and charge are shown in Fig. 10c. During the three consecutive runs, the catalytic current can readily return to its original level, thus indicating an excellent electrochemical stability of 15%-Cu/NC$_{900}$ in the ECH process.

Finally, an eight-time consecutive recycling of 15%-Cu/NC$_{900}$ was performed with the ECH of FF to probe the catalyst recyclability. Each time the 15%-Cu/NC$_{900}$ electrode was thoroughly washed and cleaned with deionized water and ethanol before the next run. Both the yields and selectivities of FA were almost unchanged during the initial seven-time recycling (Fig. 10d), thus suggesting an excellent recyclability of the 15%-Cu/NC$_{900}$. A reduced FA yield was detected at the eighth recycling due to an observed falling-off of the Cu catalyst from the carbon cloth during the long-term electrolysis (Figs. 10d and S7, Supporting Information) with vigorous stirring. Inductively coupled plasma−atomic emission spectrometry (ICP−AES) analysis of the electrolyte after the recycling experiment did not exhibit trace amount of leached Cu, thus demonstrating stability of the Cu catalyst. At the end of this

recycling experiment, a total amount of 1011 mg FA was obtained from the eight-time consecutive run. Our continuous batch electrolysis thus demonstrated potential application for large-scale production of biomass-based FA by using the developed 15%-Cu/NC$_{900}$ catalyst with excellent recyclability. Moreover, the characterizations of the recovered 15%-Cu/NC$_{900}$ showed similar results of XRD and XPS to the fresh one (Figs. S8 and S9, Supporting Information). The SEM and TEM analyses also confirmed well-maintained morphology and structure of the recovered catalyst (Fig. S8), thus suggesting an outstanding stability of the Cu electrocatalyst.

4. Conclusion

In summary, we have demonstrated Cu electrocatalyst-promoted ECH of FF to FA in aqueous KOH media in an H-type electrolytic reactor at ambient temperature. The ECH process was performed in a highly efficient and selective way by yielding a FA selectivity close to 100% with Faradaic efficiency above 95%. Moreover, the Cu catalyst shows an excellent stability and recyclability during consecutive recycling experiments. This research thus highlights a sustainable approach to electrocatalytic conversion of biomass-based compounds to high value-added products.

CRediT authorship contribution statement

Jinzhu Chen designed and directed the investigations. **Jinzhu Chen** and **Zhiyong Liu** composed the manuscript. **Wanling Xu** and **Chunjie Yu** developed the catalytic method and performed the experiments. All the authors were involved the analysis of results and discussions of the project.

Declaration of Competing Interest

The authors declare that they have no known competing financial interests or personal relationships that could have appeared to influence the work reported in this paper.

Appendix A. Supporting information

Supplementary data associated with this article can be found in the online version at doi:10.1016/j.apcatb.2022.121062.

References

[1] S. Chu, A. Majumdar, Opportunities and challenges for a sustainable energy future, Nature 488 (2012) 294–303.

[2] N.P. Martínez, M. Isaacs, K.K. Nanda, Paired electrolysis for simultaneous generation of synthetic fuels and chemicals, New J. Chem. 44 (2020) 5617–5637.

[3] Y. Zhu, Z. Li, J. Chen, Applications of lignin-derived catalysts for green synthesis, Green Energy Environ. 4 (2019) 210–244.

[4] J.C. Solarte-Toro, J.A. González-Aguirre, J.A.P. Giraldo, C.A.C. Alzate, Thermochemical processing of woody biomass: a review focused on energy-driven applications and catalytic upgrading, Renew. Sustain. Energy Rev. 136 (2021), 110376.

[5] R. Mariscal, P. Maireles-Torres, M. Ojeda, I. Sádaba, M.L. Granados, Furfural: a renewable and versatile platform molecule for the synthesis of chemicals and fuels, Energy Environ. Sci. 9 (2016) 1144–1189.

[6] Q. Wang, X. Zhuang, W. Wang, X. Tan, Q. Yu, W. Qi, Z. Yuan, Rapid and simultaneous production of furfural and cellulose-rich residue from sugarcane bagasse using a pressurized phosphoric acid-acetone-water system, Chem. Eng. J. 334 (2018) 698–706.

[7] P. Gallezot, Conversion of biomass to selected chemical products, Chem. Soc. Rev. 41 (2012) 1538–1558.

[8] K. Gupta, R.K. Rai, S.K. Singh, Metal catalysts for the efficient transformation of biomass-derived HMF and furfural to value added chemicals, ChemCatChem 10 (2018) 2326–2349.

[9] J. Anibal, B. Xu, Electroreductive C-C coupling of furfural and benzaldehyde on Cu and Pb surfaces, ACS Catal. 10 (2020) 11643–11653.

[10] N.K. Gupta, A. Fukuoka, K. Nakajima, Metal-Free and selective oxidation of furfural to furoic acid with an N-heterocyclic carbene catalyst, ACS Sustain. Chem. Eng. 6 (2018) 3434–3442.

[11] P. Zhou, Y. Chen, P. Luan, X. Zhang, Z. Yuan, S.-X. Guo, Q. Gu, B. Johannessen, M. Mollah, A.L. Chaffee, D.R. Turner, J. Zhang, Selective electrochemical hydrogenation of furfural to 2-methylfuran over a single atom Cu catalyst under mild pH conditions, Green Chem. 23 (2021) 3028–3038.

[12] J. Li, N. Kornienko, Probing electrosynthetic reactions with furfural on copper surfaces, Chem. Commun. 57 (2021) 5127–5130.

[13] J.N. Chheda, G.W. Huber, J.A. Dumesic, Liquid-phase catalytic processing of biomass-derived oxygenated hydrocarbons to fuels and chemicals, Angew. Chem. Int. Ed. 46 (2007) 7164–7183.

[14] K. Yan, A. Chen, Efficient hydrogenation of biomass-derived furfural and levulinic acid on the facilely synthesized noble-metal-free Cu-Cr catalyst, Energy 58 (2013) 357–363.

[15] J. Lee, J.H. Seo, C. Nguyen-Huy, E. Yang, J.G. Lee, H. Lee, E.J. Jang, J.H. Kwak, J. H. Lee, H. Lee, K. An, Cu2O(100) surface as an active site for catalytic furfural hydrogenation, Appl. Catal. B Environ. 282 (2021), 119576.

[16] J.G. Lee, S. Yoon, E. Yang, J.H. Lee, K. Song, H.R. Moon, K. An, Structural evolution of ZIF-67-derived catalysts for furfural hydrogenation, J. Catal. 392 (2020) 302–312.

[17] C. Xu, E. Paone, D. Rodríguez-Padrón, R. Luque, F. Mauriello, Recent catalytic routes for the preparation and the upgrading of biomass derived furfural and 5-hydroxymethylfurfural, Chem. Soc. Rev. 49 (2020) 4273–4306.

[18] J.T. Brosnahan, Z. Zhang, Z. Yin, S. Zhang, Electrocatalytic reduction of furfural with high selectivity to furfuryl alcohol using AgPd alloy nanoparticles, Nanoscale 13 (2021) 2312–2316.

[19] M.J. Islam, M.G. Mesa, A. Osatiashtiani, M.J. Taylor, J.C. Manayil, C.M.A. Parlett, M.A. Isaacs, G. Kyriakou, The effect of metal precursor on copper phase dispersion and nanoparticle formation for the catalytic transformations of furfural, Appl. Catal. B Environ. 273 (2020) 119062.

[20] C. Herrera, J. Pinto-Neira, D. Fuentealba, C. Sepúlveda, A. Rosenkranz, J.L. García-Fierro, M. González, N. Escalona, Effect of Ni metal content on emulsifying properties of Ni/CNTox catalysts for catalytic conversion of furfural in pickering emulsions, ChemCatChem 13 (2020) 682–694.

[21] A. Kumar, R. Srivastava, Pd-decorated magnetic spinels for selective catalytic reduction of furfural: interplay of a framework-substituted transition metal and solvent in selective reduction, ACS Appl. Energy Mater. 3 (2020) 9928–9939.

[22] P. Panagiotopoulou, D.G. Vlachos, Liquid phase catalytic transfer hydrogenation of furfural over a Ru/C catalyst, Appl. Catal. A Gen. 480 (2014) 17–24.

[23] J. Li, M. Zahid, W. Sun, X. Tian, Y. Zhu, Synthesis of Pt supported on mesoporous g-C3N4 modified by ammonium chloride and its efficiently selective hydrogenation of furfural to furfuryl alcohol, Appl. Surf. Sci. 528 (2020), 146983.

[24] S. Sitthisa, T. Pham, T. Prasomsri, T. Sooknoi, R.G. Mallinson, D.E. Resasco, Conversion of furfural and 2-methylpentanal on Pd/SiO2 and Pd-Cu/SiO2 catalysts, J. Catal. 280 (2011) 17–27.

[25] J. Yang, S. Li, L. Zhang, X. Liu, J. Wang, X. Pan, N. Li, A. Wang, Y. Cong, X. Wang, T. Zhang, Hydrodeoxygenation of furans over Pd-FeOx/SiO2 catalyst under atmospheric pressure, Appl. Catal. B Environ. 201 (2017) 266–277.

[26] Z. Pan, H. Jiang, B. Gong, R. Luo, W. Zhang, G.-H. Wang, Layered double hydroxide derived NiAl-oxide hollow nanospheres for selective transfer hydrogenation with improved stability, J. Mater. Chem. A 8 (2020) 23376–23384.

[27] W. Liu, Y. Wang, L. Chen, E. Xu, J. Xu, S. Hong, X. Zhang, M. Wei, Atomically-ordered active sites in NiMo intermetallic compound toward low-pressure hydrodeoxygenation of furfural, Appl. Catal. B Environ. 282 (2021), 119569.

[28] M. Stucchi, S. Alijani, M. Manzoli, A. Villa, R. Lahti, M.G. Galloni, U. Lassi, L. Prati, A Pt-Mo hybrid catalyst for furfural transformation, Catal. Today 357 (2020) 122–131.

[29] J. Zhang, J. Chen, Selective transfer hydrogenation of biomass-based furfural and 5-hydroxymethylfurfural over hydrotalcite-derived copper catalysts using methanol as a hydrogen donor, ACS Sustain. Chem. Eng. 5 (2017) 5982–5993.

[30] Y. Su, Z. Li, H. Zhou, S. Kang, Y. Zhang, C. Yu, G. Wang, Ni/Carbon aerogels derived from water induced self-assembly of Ni-MOF for adsorption and catalytic conversion of oily wastewater, Chem. Eng. J. 402 (2020), 126205.

[31] R. Bababrik, D. Santhanaraj, D.E. Resasco, B. Wang, A comparative study of thermal- and electrocatalytic conversion of furfural: methylfuran as a primary and major product, J. Appl. Electrochem. 51 (2020) 19–26.

[32] X.H. Chadderdon, D.J. Chadderdon, J.E. Matthiesen, Y. Qiu, J.M. Carraher, J. P. Tessonnier, W. Li, Mechanisms of furfural reduction on metal electrodes: distinguishing pathways for selective hydrogenation of bioderived oxygenates, J. Am. Chem. Soc. 139 (2017) 14120–14128.

[33] R.J. Dixit, K. Bhattacharyya, V.K. Ramani, S. Basu, Electrocatalytic hydrogenation of furfural using non-noble-metal electrocatalysts in alkaline medium, Green Chem. 23 (2021) 4201–4212.

[34] Y. Xu, B. Zhang, Recent advances in electrochemical hydrogen production from water assisted by alternative oxidation reactions, ChemElectroChem 6 (2019) 3214–3226.

[35] X.H. Chadderdon, D.J. Chadderdon, T. Pfennig, B.H. Shanks, W. Li, Paired electrocatalytic hydrogenation and oxidation of 5-(hydroxymethyl)furfural for efficient production of biomass-derived monomers, Green Chem. 21 (2019) 6210–6219.

[36] J.J. Roylance, T.W. Kim, K.-S. Choi, Efficient and selective electrochemical and photoelectrochemicalreduction of 5-hydroxymethylfurfural to 2,5-bis(hydroxymethyl)furan using water as the hydrogen source, ACS Catal. 6 (2016) 1840–1847.

[37] A.S. May, E.J. Biddinger, Strategies to control electrochemical hydrogenation and hydrogenolysis of furfural and minimize undesired side reactions, ACS Catal. 10 (2020) 3212–3221.

[38] S.A. Akhade, N. Singh, O.Y. Gutiérrez, J. Lopez-Ruiz, H. Wang, J.D. Holladay, Y. Liu, A. Karkamkar, R.S. Weber, A.B. Padmaperuma, M.-S. Lee, G.A. Whyatt, M. Elliott, J.E. Holladay, J.L. Male, J.A. Lercher, R. Rousseau, V.-A. Glezakou, Electrocatalytic hydrogenation of biomass-derived organics: a review, Chem. Rev. 120 (2020) 11370–11419.

[39] P. Nilges, U. Schröder, Electrochemistry for biofuel generation: production of furans by electrocatalytic hydrogenation of furfurals, Energy Environ. Sci. 6 (2013) 2925–2931.

[40] W. Chen, C. Xie, Y. Wang, Y. Zou, C. Dong, Y. Huang, Z. Xiao, Z. Wei, S. Du, C. Chen, B. Zhou, J. Ma, S. Wang, Activity origins and design principles of Nickel-based catalysts for nucleophile electrooxidation, Chem 6 (2020) 2974–2993.

[41] X. Chong, C. Liu, Y. Huang, C. Huang, B. Zhang, Potential-tuned selective electrosynthesis of azoxy-, azo- and amino-aromatics over a CoP nanosheet cathode, Natl. Sci. Rev. 7 (2020) 285–295.

[42] C. Yang, X. Li, Z. Zhang, B. Lv, J. Li, Z. Liu, W. Zhu, F. Tao, G. Lv, Y. Yang, High efficient catalytic oxidation of 5-hydroxymethylfurfural into 2,5-furandicarboxylic acid under benign conditions with nitrogen-doped graphene encapsulated Cu nanoparticles, J. Energy Chem. 50 (2020) 96–105.

[43] Y. Wu, C. Liu, C. Wang, S. Lu, B. Zhang, Selective transfer semihydrogenation of alkynes with H2O (D2O) as the H (D) source over a Pd-P cathode, Angew. Chem. Int. Ed. 59 (2020) 21170–21175.

[44] D. Li, J. Zhang, Y. Liu, H. Yuan, Y. Chen, Boron doped magnetic catalysts for selective transfer hydrogenation of furfural into furfuryl alcohol, Chem. Eng. Sci. 229 (2021), 116075.

[45] H. Wu, J. Song, C. Liu, Z. Xie, C. Xie, Y. Hu, X. Huang, M. Hua, B. Han, An electrocatalytic route for transformation of biomass-derived furfural into 5-hydroxy-2(5H)-furanone, Chem. Sci. 10 (2019) 4692–4698.

[46] S. Li, X. Sun, Z. Yao, X. Zhong, Y. Cao, Y. Liang, Z. Wei, S. Deng, G. Zhuang, X. Li, J. Wang, Biomass valorization via paired electrosynthesis over vanadium Nitride-based electrocatalysts, Adv. Funct. Mater. 29 (2019), 1904780.

[47] Y. Cao, J. Knijff, A. Delparish, M.F.N. d'Angelo, L. Noël, A divergent paired electrochemical process for the conversion of furfural using a divided-cell flow microreactor, ChemSusChem 14 (2020) 590–594.

[48] S.K. Green, J. Lee, H.J. Kim, G.A. Tompsett, W.B. Kim, G.W. Huber, The electrocatalytic hydrogenation of furanic compounds in a continuous electrocatalytic membrane reactor, Green Chem. 15 (2013) 1869–1879.

[49] P. Parpot, A.P. Bettencourt, G. Chamoulaud, K.B. Kokoh, E.M. Belgsir, Electrochemical investigations of the oxidation–reduction of furfural in aqueous medium: application to electrosynthesis, Electrochim. Acta 49 (2004) 397–403.

[50] M. Cai, Y. Zhang, Y. Zhao, Q. Liu, Y. Li, G. Li, Two-dimensional metal-organic framework nanosheets for highly efficient electrocatalytic biomass 5-(hydroxymethyl)furfural (HMF) valorization, J. Mater. Chem. A 8 (2020) 20386–20392.

[51] B. Garlyyev, S. Xue, J. Fichtner, A.S. Bandarenka, C. Andronescu, Prospects of value-added chemicals and hydrogen via electrolysis, ChemSusChem 13 (2020) 2513–2521.

[52] Z.W. Seh, J. Kibsgaard, C.F. Dickens, I. Chorkendorff, J.K. Nørskov, T.F. Jaramillo, Combining theory and experiment in electrocatalysis: Insights into materials design, Science 355 (2017) eaad4998.

[53] Q. He, D. Tian, H. Jiang, D. Cao, S. Wei, D. Liu, P. Song, Y. Lin, L. Song, Achieving efficient alkaline hydrogen evolution reaction over a Ni5P4 catalyst incorporating single-atomic Ru sites, Adv. Mater. 32 (2020), 1906972.

[54] T. Rajala, R. Kronberg, R. Backhouse, M.E.M. Buan, M. Tripathi, A. Zitolo, H. Jiang, K. Laasonen, T. Susi, F. Jaouen, T. Kallio, A platinum nanowire electrocatalyst on single-walled carbon nanotubes to drive hydrogen evolution, Appl. Catal. B Environ. 265 (2020), 118582.

[55] E. Andrews, J.A. Lopez-Ruiz, J.D. Egbert, K. Koh, U. Sanyal, M. Song, D. Li, A. J. Karkamkar, M.A. Derewinski, J. Holladay, O.Y. Gutiérrez, J.D. Holladay, Performance of base and noble metals for electrocatalytic hydrogenation of bio-oil-derived oxygenated compounds, ACS Sustain. Chem. Eng. 8 (2020) 4407–4418.

[56] B. Wu, N. Zheng, Surface and interface control of noble metal nanocrystals for catalytic and electrocatalytic applications, Nano Today 8 (2013) 168–197.

[57] S.R. Kubota, K.-S. Choi, Electrochemical valorization of furfural to maleic acid, ACS Sustain. Chem. Eng. 6 (2018) 9596–9600.

[58] G.S. de Luna, P.H. Ho, A. Lolli, F. Ospitali, S. Albonetti, G. Fornasari, P. Benito, Ag electrodeposited on Cu open-cell foams for the selective electroreduction of 5-hydroxymethylfurfural, ChemElectroChem 7 (2020) 1238–1247.

[59] L. Zhang, F. Zhang, F.C. Michel, A.C. Co, Efficient electrochemical hydrogenation of 5-hydroxymethylfurfural to 2,5-Bis(hydroxymethyl)furan on Ag-displaced nanotextured Cu catalysts, ChemElectroChem 6 (2019) 4739–4749.

[60] H. Xie, T. Wang, J. Liang, Q. Li, S. Sun, Cu-based nanocatalysts for electrochemical reduction of CO2, Nano Today 21 (2018) 41–54.

[61] S. Jung, A.N. Karaiskakis, E.J. Biddinger, Enhanced activity for electrochemical hydrogenation and hydrogenolysis of furfural to biofuel using electrodeposited Cu catalysts, Catal. Today 323 (2019) 26–34.

[62] L. Liu, H. Liu, W. Huang, Y. He, W. Zhang, C. Wang, H. Lin, Mechanism and kinetics of the electrocatalytic hydrogenation of furfural to furfuryl alcohol, J. Electroanal. Chem. 804 (2017) 248–253.

[63] X. Zhang, M. Han, G. Liu, G. Wang, Y. Zhang, H. Zhang, H. Zhao, Simultaneously high-rate furfural hydrogenation and oxidation upgrading on nanostructured transition metal phosphides through electrocatalytic conversion at ambient conditions, Appl. Catal. B Environ. 244 (2019) 899–908.

[64] M. Chen, Q. Wu, C. Lin, J. Zhang, J. Zhao, J. Chen, Y. Xu, Chemical fixation of CO_2 using highly dispersed Cu on hierarchically porous N-doped carbon, ACS Appl. Mater. Interfaces 12 (2020) 40236–40247.

[65] M.S. Abaee, R. Sharifi, M.M. Mojtahedi, Room-Temperature cannizzaro reaction under mild conditions facilitated by magnesium bromide ethyl etherate and triethylamine, Org. Lett. 7 (2005) 5893–5895.

[66] T.A. Geissman, The cannizzaro reaction, Org. React. 2 (1944) 94–113.

[67] A.E. Russell, S.P. Miller, J.P. Morken, Efficient lewis acid catalyzed intramolecular cannizzaro reaction, J. Org. Chem. 65 (2000) 8381–8383.

[68] F. Wang, M. Xu, L. Wei, Y. Wei, Y. Hu, W. Fang, C.G. Zhu, Fabrication of La-doped TiO_2 film electrode and investigation of its electrocatalytic activity for furfural reduction, Electrochim. Acta 153 (2015) 170–174.

[69] J. Tan, W. Zhang, Y. Shu, H. Lu, Y. Tang, Q. Gao, Interlayer engineering of molybdenum disulfide toward efficient electrocatalytic hydrogenation, Sci. Bull. 66 (2021) 1003–1012.